Determination of volumetric plasma parameters from spectroscopic N II and N III line ratio measurements in the ASDEX Upgrade divertor

S. S. Henderson[1], M. Bernert[2], S. Brezinsek[3], M. Carr[4], M. Cavedon[2], R. Dux[2], B. Lipschultz[5], M. G. O'Mullane[1], F. Reimold[2], M. L. Reinke[6], the ASDEX Upgrade team[2], and the MST1 team‡

[1] Department of Physics SUPA, University of Strathclyde, Glasgow, G4 0NG, UK
[2] Max-Planck-Institut für Plasmaphysik, D-85748 Garching, Germany
[3] Forschungszentrum Juelich GmbH, Trilateral Euregio Cluster, 52425 Juelich, Germany
[4] CCFE, Culham Science Centre, OX14 3DB, UK
[5] University of York, York Plasma Institute, Heslington, York, YO10 5DD, UK
[6] Oak Ridge National Laboratory, Oak Ridge, TN 37831, USA

E-mail: stuart.s.henderson@strath.ac.uk

Abstract. The diagnosis of tokamak divertor plasmas is limited in the ability to understand the behaviour and role of impurities, central to the overall understanding of how the divertor plasma can be utilised to control the power exhaust. New methods have been developed to extract the N concentration as well as plasma characteristics; the use of three visible N II lines has been shown to provide a unique solution of the background plasma density and temperature. Those techniques are applied to data from two sightlines sampling horizontally across the outer divertor plasma. The plasma densities obtained from the N II line ratios during a scan of the divertor temperature in a partially detached H-mode plasma suggest that, as the temperature drops, the plasma density decreases further up the divertor leg while closer to the strike point the plasma density increases. The former is consistent with the emission zone moving from the private flux region into the scrape-off-layer plasma, and therefore sampling two different density regimes, while the latter is consistent with electron pressure conservation along a field line. With an approximate model of the length of the emission region, the N II divertor concentration is calculated in this discharge to be $\approx 5 - 25\%$. The single N III line ratio measurement available within the same spectral range is dependent on temperature and density and therefore cannot provide a unique solution of both.

1. Introduction

The plasma parameters in the scrape-off-layer (SOL) and private flux region (PFR) of a tokamak calculated in modelling codes, such as SOLPS5.0, are generally constrained

‡ See author list of H. Meyer et al 2017 Nucl. Fusion 57 102014

by comparisons with poloidal distributions of the total radiated power inferred from inverted bolometric measurements and with divertor Langmuir probe measurements [1–3]. Spectroscopic studies of emission from neutral atoms can offer a non-invasive means for diagnosing the divertor plasma conditions, such as the broadening of Balmer lines due to the Stark effect [4, 5] to determine the electron density and the ratio of the discrete-to-continuum background emission to indicate the electron temperature [6]. With the development of impurity seeding scenarios to moderate the divertor heat flux in tokamaks [7–11], there is now more opportunity to diagnose the emission from the injected impurity ions to characterise the background plasma conditions in hotter regions of the SOL and PFR where neutrals are less prevalent. Furthermore, SOL modelling of nitrogen seeded H-mode plasmas is an active area of research [12] which could benefit from the spectroscopic constraints listed above, and also from the comparison of different charge state emission along an array of sightlines providing a gauge of the impurity transport and fraction in the SOL [13–15].

This paper aims to build upon the current spectral analysis techniques that focus on Balmer emission by modelling the sensitivity of different N II and N III intensities to the electron temperature and density. Since nitrogen is used routinely for divertor protection control in ASDEX Upgrade (AUG) [16], measurements of nitrogen emission are generally available in most AUG discharges. Furthermore, N II and N III feature a number of intense lines within the same visible spectral range routinely used to measure the Stark broadening of the D_δ and D_ϵ Balmer lines [4]. It is shown in this paper that by measuring the intensity of three N II lines in this spectral range, a single solution of the electron density and temperature can be inferred. A model of the length and location of the emitting region is also discussed and used to infer the N II concentration in the divertor during an ELMy H-mode AUG discharge.

The paper is organised as follows. In section 2, the plasma conditions and divertor spectroscopy setup is described along with a summary of the spectral fitting post-processing and an overview of the emission zones. The atomic data required for the collisional radiative modelling of the N II and N III radiance is described in section 3. The modelled line ratios are presented in section 3.3 with a discussion of the uncertainties from the ionisation balance given in section 3.4. The measurements of the electron temperature and density, and an estimation of the N II divertor concentration is given in section 4. A method for implementing such a line ratio technique as a constraint in a SOL model or as a control-room analysis technique is also given in this section. Lastly, the conclusions of the paper are given in section 5.

2. Experimental setup and measurements

The ELMy H-mode AUG discharge #32244 is used to demonstrate the spectral analysis of N II and N III in the outer divertor plasma region. The discharge was run in lower single null configuration with a total heating power of $P_{heat} = 16.6$ MW, a plasma current of $I_p = 1$ MA with a flat-top time from $t = 2 - 7$ s, and a toroidal magnetic field

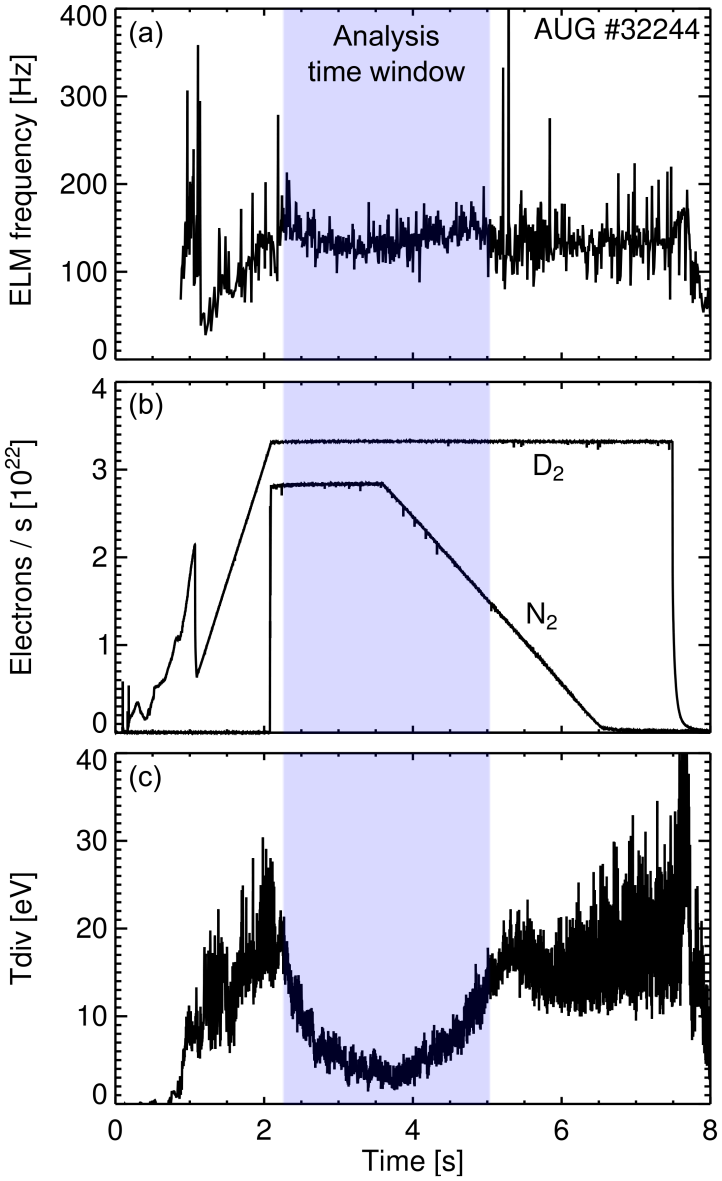

Figure 1. The ELM frequency (a), the D_2 and N_2 fuelling/seeding rate (b), and the outer divertor target temperature (c) are shown for AUG discharge #32244. The time window used for the analysis in this paper is represented by the shaded region.

of $B_t = 2.5$ T. This discharge is of particular interest due to the relatively low ELM frequency $f_{ELM} \sim 130$ Hz and the partial detachment of the outer divertor leg [17] which both facilitate the analysis of inter-ELM low charge state impurity emission. The ELM frequency determined by the divertor current, the D_2 and N_2 fuelling/seeding rate, and the inter-ELM outer divertor target temperature T_{div} derived from thermocurrents [16] are shown in figures 1a, b, and c, respectively.

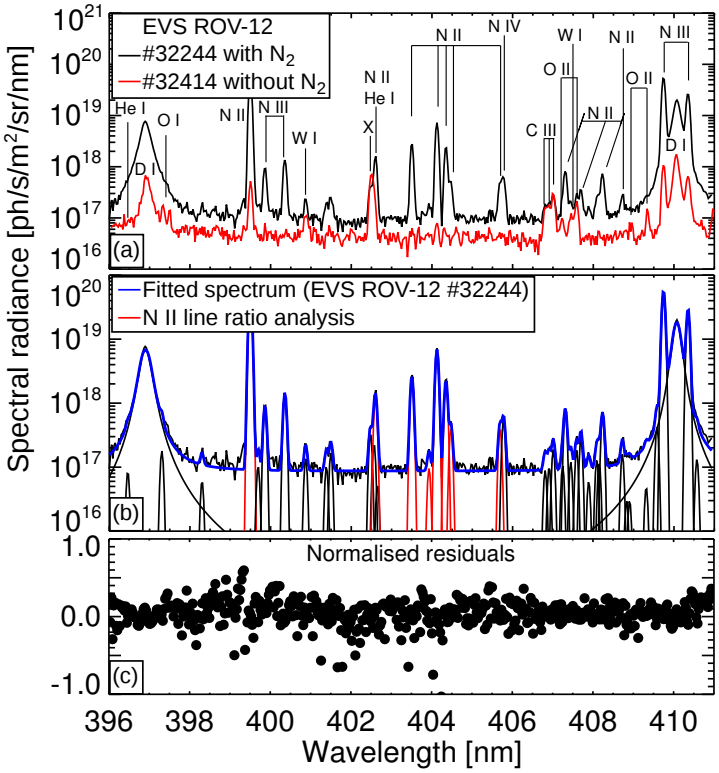

Figure 2. Time-averaged spectrum measured in ROV-12 with (#32244 averaged over analysis time window, black) and without (#32414 averaged over I_p flat-top, red) N_2 seeding is shown in (a). Line identifications are based on modelling results and the NIST database. An example of the fitted spectrum from #32244 is shown in (b) with the normalised residuals shown in (c).

2.1. Divertor spectroscopy setup

Routinely on AUG, the divertor Czerny Turner-like visible spectrometer is used to evaluate the Stark broadening of the D_ϵ and D_δ spectral lines [4]. In this setting, the spectrometer is set with a centre wavelength of $\lambda_0 = 403.6$ nm, a spectral range of 395.995 nm $\leq \lambda \leq$ 410.939 nm, and an integration time of $\Delta t = 2.5$ ms. This spectral range is also useful for analysis of nitrogen emission, in addition to a number of other impurity lines of interest. An example time-averaged spectrum measured across the outer divertor (from the ROV-12 sightline) during #32244 is shown in figure 2a. The equivalent spectrum measured during AUG discharge #32414 with no N_2 seeding and low intrinsic nitrogen concentration is shown by the red curve. In #32414, T_{div} is ≈ 20 eV over the entire I_p flat-top time and therefore represents similar conditions to the start and end T_{div} in the time window analysed in this paper. The line identification summarised in table 1 is based on lines from the online NIST database [18] and from lines predicted by the atomic model described in section 3.

2.2. Spectral fitting

The analysis in this paper focuses on the spin-orbit ls multiplet radiance from the N II emission at 399.5 nm (one line), 402.6 nm (two lines), and 404.1 nm (five lines) and from the N III emission at 400.0 nm (two lines) and 410.0 nm (one line). Fitting of the background and line emission is performed in this analysis using the Framework for Feature Synthesis (FFS) routines [19] which are available as part of the ADAS code library. In the FFS, a model file describing the spectrum with a list of functions is first prescribed following the format of the LISt Processor language (LISP) syntax [20]. These functions include a Gaussian and Voigtian broadening function and a linear background function. The free parameters associated with the functions are then varied using a least squares (Levenberg-Marquardt) algorithm to minimise the (χ^2_N) difference between the measured and modelled spectral radiance. The Voigtian is split into a Gaussian line shape and a Lorentzian line shape whose full width at half maximum (FWHM) depends upon the electron density using the tables provided in [5]. An example of the fit is shown in figure 2b with normalised residuals shown in figure 2c.

The ratios of the lines within these multiplets are approximately independent of the background plasma and can therefore be measured experimentally. To reduce the number of free fitting parameters, the ls coupling ratios are fixed to the experimental measurements shown in table 1 and the FWHM is fixed to the instrument function 0.08 nm (Doppler broadening is negligible for these low charge lines). The N II lines at

Table 1. Identified transitions and measured ls coupling ratios.

Ion	Transition	Wavelength air [nm]	Fit coupling ratio
N II	$2p3p\ ^1D_2 \rightarrow 2p3s\ ^1P_1$	399.500	1.000
N III	$2s^25f\ ^2F_{2.5} \rightarrow 2s^24d\ ^2D_{1.5}$	399.863	0.375
N III	$2s^25f\ ^2F_{3.5} \rightarrow 2s^24d\ ^2D_{2.5}$	400.358	0.625
W I	$5d^46s\ 6p\ ^7P_4 \rightarrow 5d^56s\ ^7S_3$	400.875	1.000
X	–	402.478	0.541
X	–	402.533	0.373
He I	$2p3p\ ^1D_2 \rightarrow 2p3s\ ^1P_1$	402.622	0.086
N II	$2p4f\ ^1G_4 \rightarrow 2p3d\ ^3F_3$	402.609	0.944
N II	$2p4f\ ^1G_4 \rightarrow 2p3d\ ^3F_4$	403.935	0.056
N II	$2p4f\ ^3G_3 \rightarrow 2p3d\ ^3F_2$	403.509	0.205
N II	$2p4f\ ^3G_5 \rightarrow 2p3d\ ^3F_4$	404.132	0.562
N II	$2p4f\ ^3G_4 \rightarrow 2p3d\ ^3F_3$	404.354	0.175
N II	$2p4f\ ^3G_3 \rightarrow 2p3d\ ^3F_3$	404.479	0.029
N II	$2p4f\ ^3G_4 \rightarrow 2p3d\ ^3F_4$	405.692	0.029
N IV	$2p4f\ ^3G_4 \rightarrow 2p3d\ ^3F_4$	405.776	1.000
N III	$2s^23p\ ^2P_{1.5} \rightarrow 2s^23s\ ^2S_{0.5}$	409.733	0.667
N III	$2s^23p\ ^2P_{0.5} \rightarrow 2s^23s\ ^2S_{0.5}$	410.343	0.333

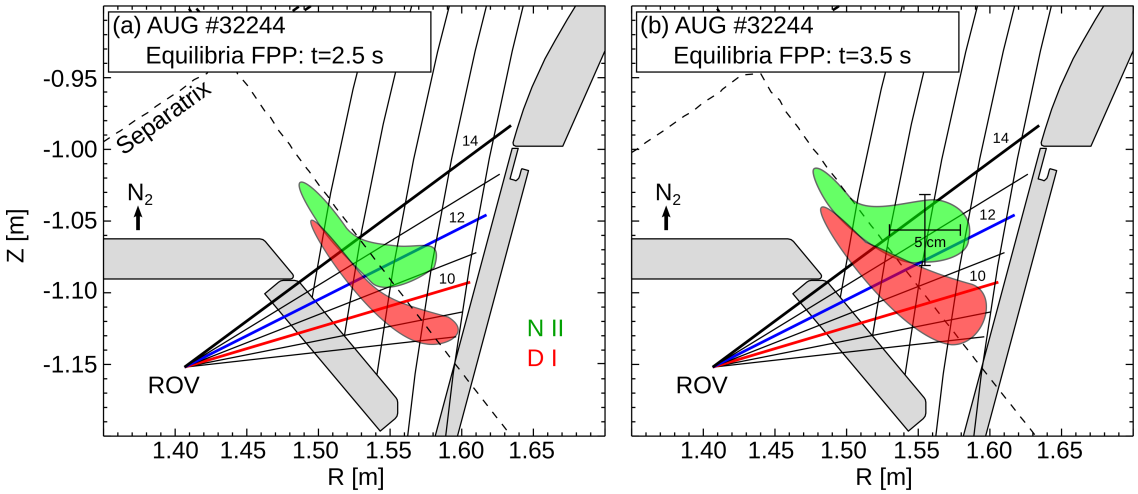

Figure 3. A poloidal cross-section of the AUG divertor region showing a subset of the total number of available spectrometer sightlines. The sightlines in bold colour indicate those used for analysis in this paper. The evolution of the N II (green) and D I (red) inter-ELM emission zones are shown (a) when $T_{div} \approx 10$ eV and (b) when $T_{div} < 5$ eV during the analysis time window.

399.5 nm and 404.1 nm are relatively bright, in comparison to other lines and to the background, and therefore the fitting of their Gaussian intensities is generally robust. The N II line at 402.6 nm is relatively weak in comparison and has three possible contaminating impurity lines nearby: two unidentified lines at 402.4 nm and 402.5 nm, and a He I line at 402.6 nm. The latter He I line is not *ls* coupled to any other line in this spectra, however it should approximately correlate in intensity with the He I line at 396.4 nm. Since this lower wavelength He I line at 396.4 nm is not visible in the spectrum measured during #32244, it is assumed that the He I line at 402.6 nm does not contribute to the background feature near 402.5 nm. Previous literature suggests that the remaining two impurity lines are C II lines [21], however they do not appear to correlate with other carbon lines in the spectra, nor do they increase with the He I emission. In this analysis, the coupling between the two unidentified lines (marked by X in table 1) is measured during #32414 and then applied to the fit in the analysis of #32244. The remaining N II lines at higher wavelength can in principle be analysed, however these lines are also weak and heavily mixed with other W I, D I, C II, and O II emission making their interpretation challenging.

2.3. Emission zones

For the analysis in this paper, the location and extent of the emission zone for each species is required to calculate the length of the emitting region along a sightline (for determination of the impurity concentration, see section 4.1) and to localise the region of plasma density and temperature characterising the emission. To determine these zones requires either an inversion of a filtered camera image or alternatively there is the possibility of tomographic analysis of the divertor using the full range of spectrometer

sightlines available on AUG [12]. The former technique provides the largest number of line-of-sights (LOS) to constrain the inversion provided that parasitic background lines can be excluded in the bandwidth of the filter; however in the visible spectral range there is the severe issue of reflections in a metal wall environment which must be accounted for [22]. Reflections are less of an issue for the spectrometer views on AUG as they end in viewing dumps [4]; however the number of LOSs are often limited by the spectrometer settings. Ideally, this type of spectroscopic analysis is most powerful with the combination of both filtered camera images and spectrometers. For AUG discharge #32244, filtered camera images were not available and only a subset of the total number of spectrometer LOSs were setup as described in the previous section. Therefore an approximation of the N II and D I emission zones are made using LOS-based localization of the inter-ELM emission from the available horizontal (ROV-##) and vertical (DOT-##) sightlines shown in figure 3. Using this technique provides a constraint on the emission zone location which is accurate to ≈ 2 cm.

An illustration of the emission zones are shown for two different times, $t \approx 2.5$ s and $t \approx 3.5$ s, in figures 3a and b respectively. At $t \approx 2.5$ s the N II and D I (inter-ELM) emission measured through ROV-14 is located mainly in the private flux region (PFR). In ROV-12 the N II emission is spread further into the SOL whereas the D I emission is confined to the PFR and the region in front of the divertor tile. At $t \approx 3.5$ s there is a shift in N II emission from ROV-12 to ROV-14 suggesting a movement of the N II emission zone towards the X-point. This temporal evolution of the emission is consistent with previous modelling of high-recycling, partially detached plasma [2, 12].

The horizontal outer divertor ROV sightlines are useful for benchmarking the atomic data since the sightlines integrate through only a small section of plasma in the outer divertor where, as discussed above, the emission is modelled to be approximately localised to the PFR. The specific sightlines analysed in this paper, ROV-12 and ROV-14, are shown by the blue and black bold lines in figure 3a, respectively. The seeding valve, located in the PFR as indicated in figure 3a, and the spectrometer sightlines are in a different toroidal sectors and therefore the results presented in this paper assume toroidally symmetric emission.

2.4. Inter-ELM measurements

The fitted N II 399.5 nm radiance is shown in figure 4a as a coherently ELM-averaged signal (for the above described discharge) between 2.3 s<t< 5.0 s and for sightlines ROV-10, ROV-12, and ROV-14. Since the integration time of the spectrometer is relatively long in comparison to the ELM time (t_{res}=2.5 ms), it is important to assess the impact of this on inter-ELM measurements. The time base of the spectrometer (t_b) indicates the start of the integration interval. In this analysis, the spectrometer time base is adjusted to $t_n = t_b + t_{res}/2$ to reduce the likelihood of misinterpreting ELM and inter-ELM measurements. The effect of this shift, in addition to the temporal instrument function, leads to 2.5 ms wide (and 1.25 ms delayed) trapeze. Inter-ELM measurements

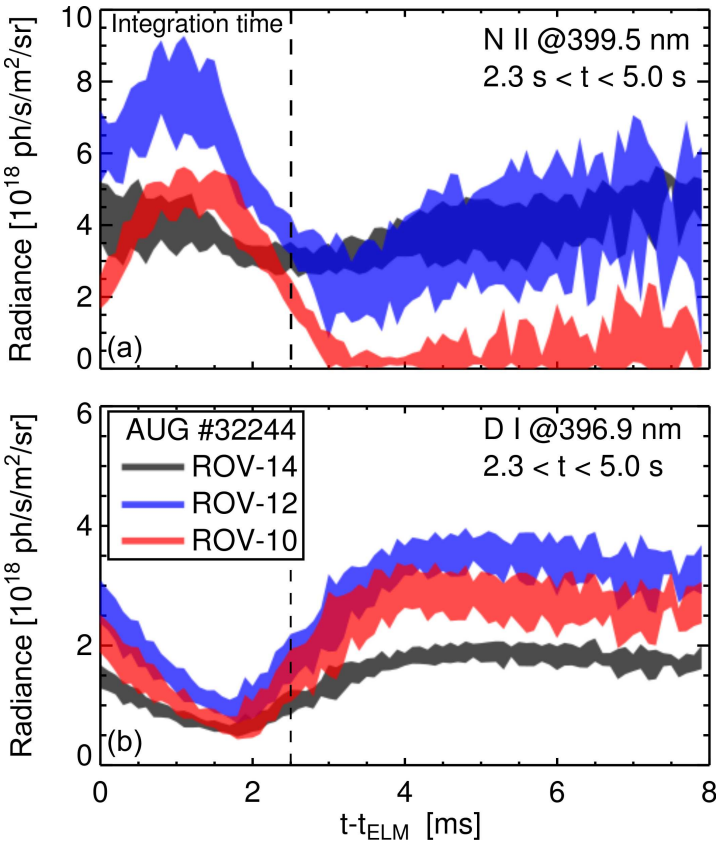

Figure 4. The coherently ELM-averaged signal of the N II and D I radiance at 399.5 nm and 396.9 nm respectively is shown for discharge #32244 in (a) and (b). The time base of the spectrometer has been normalised to start time of the ELM with a 1.25 ms shift (see text) and the shaded curves represent the standard deviation of the data binned over 0.2 ms for ROV-14 (black), ROV-12 (blue), ROV-10 (red).

are defined here as 4.5 ms after the ELM start time to avoid measuring emission during the ELM and to allow for a short recovery period immediately after the ELM. The inter-ELM N II radiance from ROV-14 is relatively strong, whereas there is virtually no analysable inter-ELM measurement for ROV-10 in this time window. The D I radiance shown on the same x-axis in figure 4b evolves on a similar timescale to the N II radiance after the ELM, but with the opposite trend during and immediately after the ELM.

The inter-ELM spectral radiance is binned over 12 time frames giving a temporal resolution of ~ 30 ms which is sufficient to produce a robust fit whilst not significantly distorting the measurement. Figure 5a and 5b show an example of the inter-ELM N II 404.1 / 399.5 nm and N III 400.0 / 410.0 nm line ratios, respectively, as a function of time for ROV-12 and ROV-14. The N II line ratio decreases with T_{div} in ROV-14, whereas in ROV-12 the ratio increases with T_{div} for $T_{div} < 8$ eV. A similar evolution is also found in the N III line ratio measurements. It is shown in the next section that these particular N II and N III line ratios both increase with T_e and n_e meaning that, if the temperature of the emitting zone doesn't change significantly, then this ratio is effectively providing a measurement of n_e.

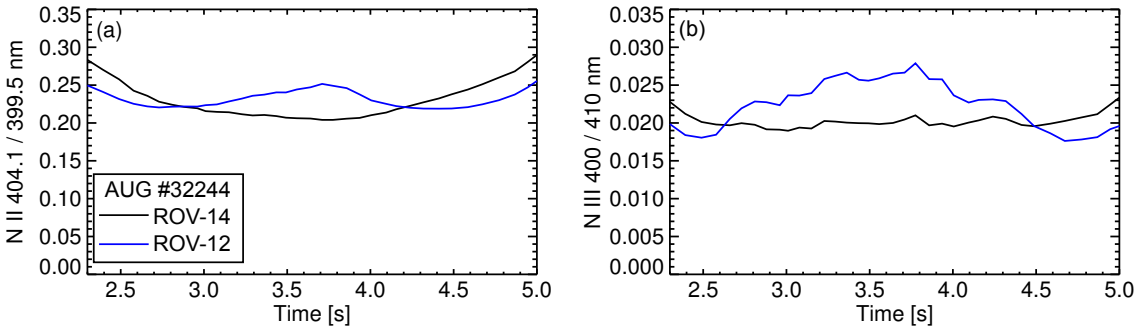

Figure 5. The temporal evolution of the inter-ELM ($t - t_{ELM} > 4.5$ ms) N II and N III line ratios for two divertor sight lines. The changes in the ratios represent the evolution of the temperature and density during the analysis time window.

3. Atomic data

To model the impurity line emission the atomic data required are the spontaneous radiative decay rates (A-values), the Maxwellian averaged electron excitation rate coefficients from the ground to the metastable and diagnostically relevant upper excited states, and the ionisation and recombination rate coefficients to determine the balance between the excitation and recombination driven emission. More accurately, the (de-)excitation collision strengths between all levels should be included and modelled using a collisional radiative population model [23]. This latter technique is used in this paper with atomic data inputs described in the following subsections.

3.1. N II

Effective (Maxwellian averaged) collision strengths calculated by Tayal [24] in the close-coupling approximation using the B-spline Breit-Pauli R-matrix method have been collected and archived in ADAS data format (see Appendix A.1). The effective collision strengths are tabulated at temperatures ranging from $0.04 - 8.62$ eV for 1653 fine-structure transitions among the 58 target levels belonging to the ground and excited configurations: $2s^22p^2$, $2s^22p3s$, $2s^22p3p$, $2s^22p3d$, $2s^22p4s$, $2s^22p4p$, $2s2p^3$, and $2s2p^23s$. Only electric dipole (E1) spontaneous emission coefficients A are provided from this data source, therefore values for the remaining transitions are supplemented from the CHIANTI database [25]. The energies of the 58 target levels are taken from NIST.

To model the N II spectrum shown in figure 2, this data set must be expanded to include equivalent data for the $2s^22p4d$ and $2s^22p4f$ configurations. The energies of the additional 24 fine structure levels are included in the offline NIST documentation [26]. The effective collision strengths, spontaneous emission coefficients and level energies for the expanded data set have been calculated for this analysis in the distorted wave approximation using the semi-relativistic *autostructure* code [27] (AS). The optimisation of the orbital radial scaling parameters in AS is described in Appendix A.

A widely recognised quality gauge for the optimisation is generally a comparison of

the energy levels with NIST and a comparison of the weighted oscillator strengths gf calculated in the velocity and length formulations [28, 29]. The A-values, gf velocity and length ratio, and the wavelengths for the three N II transitions used in this analysis are shown in table 2. The A-values in bold are recommended values; the recommended A-value for the N II 399.5 nm line is taken from literature [24] and the other two are guided by the constraints imposed by spectral measurements. The difference between the recommended and calculated A-values for the 4f−3d transitions are within the equivalent error found for the 3p−3s. An uncertainty of $< 25\%$ in the A-value, coupled with the close agreement of the two formulations of the weighted oscillator strengths and of the NIST energy levels, indicates that the uncertainty in the population of the 4f terms from the collision strengths is negligible compared to the measurement and modelling (see section 3.4) uncertainties.

3.2. N III

For N III, the atomic data set used is based on a collection of (Maxwellian averaged) collision strengths [30], A-values [31], and energy levels from NIST including configurations up to the 4f shell. To model the 400 nm N III line, the data set was supplemented with transition data spanning up to the 5g shell calculated by the *cowan* atomic structure code [32] with plane-wave Born collision strengths. The default *cowan* calculation provides a sufficiently low uncertainty on the atomic structure due to the higher charge of the ion. The calculated A-value for the 400.0 nm transition (2.17 10^8 s^{-1}) has been updated to the value recommended by NIST (1.88 10^8 s^{-1}).

3.3. Line ratio model

The total emissivity for each transition is defined as

$$\epsilon_{j\to i} = A_{j\to i} n_e \left(\sum_{\sigma} n_{\sigma Z} f^{exc}_{\sigma j} + \sum_{\mu} n_{\mu Z+1} f^{rec}_{\mu j} \right) \ [\mathrm{ph/s/m^{-3}}] \tag{1}$$

where j and i represent the upper and lower levels of the transition, σ and μ represent the ground and metastable levels of the $n_{\sigma Z}$ and $n_{\sigma Z+1}$ ion densities respectively, and $f^{exc,rec}_{\sigma j}$ is the fractional bound population of the excited state driven by excitation and recombination. The generalised collisional radiative (GCR) model in ADAS (called ADAS208) is used to calculate $f^{exc,rec}_{\sigma j}$ using the fundamental data described in the

Table 2. Fundamental data from an optimised Autostructure (AS) structure calculation of N II.

Transition	$\frac{\lambda_{AS}}{\lambda_{NIST}}$	$gf_{vel/len}$	$A^{AS,\mathbf{rec}}$ [10^8 s^{-1}]
2p3p ^{1}D → 2p3s ^{1}P	0.922	0.994	1.59, **1.30**
2p4f ^{1}G → 2p3d ^{3}F	1.017	1.019	0.67, **0.87**
2p4f ^{3}G → 2p3d ^{3}F	1.018	1.015	2.07, **1.69**

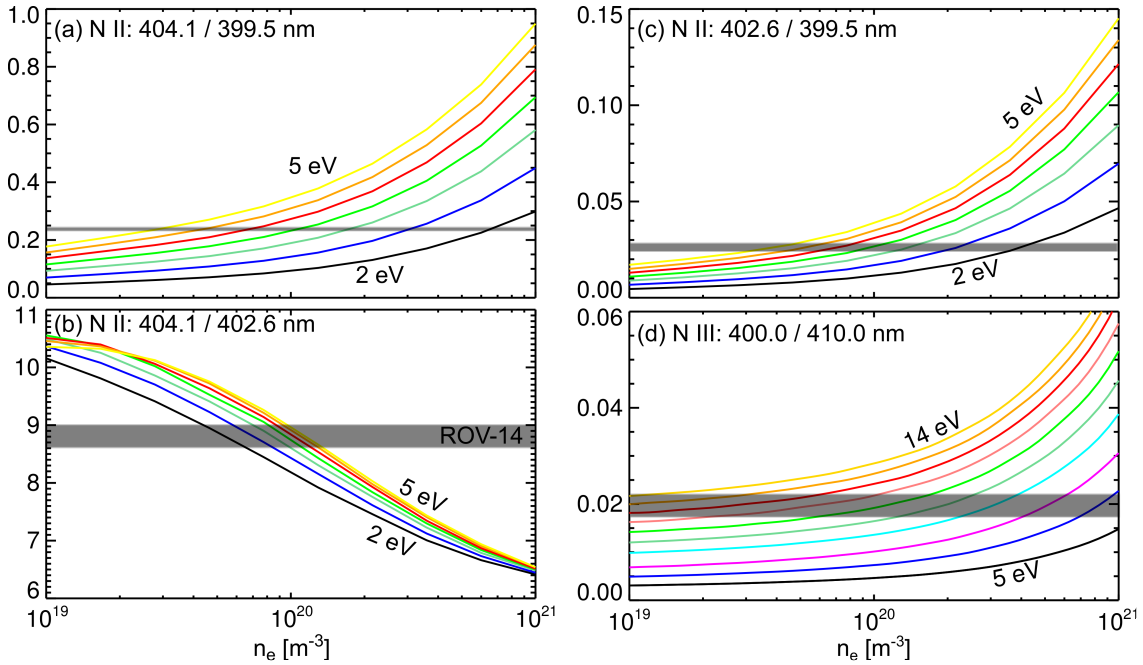

Figure 6. Predictions of three different N II line ratios are shown as a function of electron density in (a)-(c) and of one N III line ratio in (d). The different curves in each plot indicate a change in temperature, with increments of 0.5 eV starting at 2 eV in (a)-(c) and of 1 eV starting 5 eV in (d). An unresolved, zero-transport ionisation balance has been used to model the balance between excitation and recombination driven emission. The shaded regions represent the measured line ratios through ROV-14 at t=3.0 s.

previous subsection in *ls* resolution. The contribution from the highly excited Rydberg states are calculated in the bundle-n approach and then condensed and projected on to the set of *ls* target states using the projection matrices of GCR theory [23].

An unresolved ionisation balance (treating all metastables as ordinary excited levels in equilibrium with the ground state) is used to model the equilibrium fractional abundance of N II and N III. In this zero-transport, unresolved, equilibrium approximation the N II and N III emissivity should respectively peak over a narrow temperature range of $T_e \sim 3-4$ eV (with a wider emission range of $T_e \sim 2-8$ eV) and $T_e \sim 6$ eV (with a wider emission range of $T_e = 3-15$ eV).

The ratio of the N II $\epsilon_{j\to i}$ emissivities for 404.1/399.5 nm, 404.1/402.6 nm, and 402.6/399.5 nm are shown in figures 6a-c, respectively; the line ratios in 6a divided by those in 6b are equal to those shown in 6c. Measuring multiple line ratios allows for an exact solution of T_e and n_e and, since the A-values are not dependent on T_e and n_e and therefore only act as a linear multiplier on each ratio, provide a constraint for the A-value solution (i.e. the basis for $A^{\mathbf{rec}}$ in table 2). In figures 6a-c, the measured ratio values from ROV-14 at t=3.0 s used to constrain the A-values are shown for comparison. The ratio of the N III $\epsilon_{j\to i}$ emissivities for 400.0/410.0 nm are shown in figure 6d as a function of n_e for a range of T_e. The N III line ratio is sensitive to both T_e and n_e therefore a single solution of T_e and n_e from N III is not possible without additional

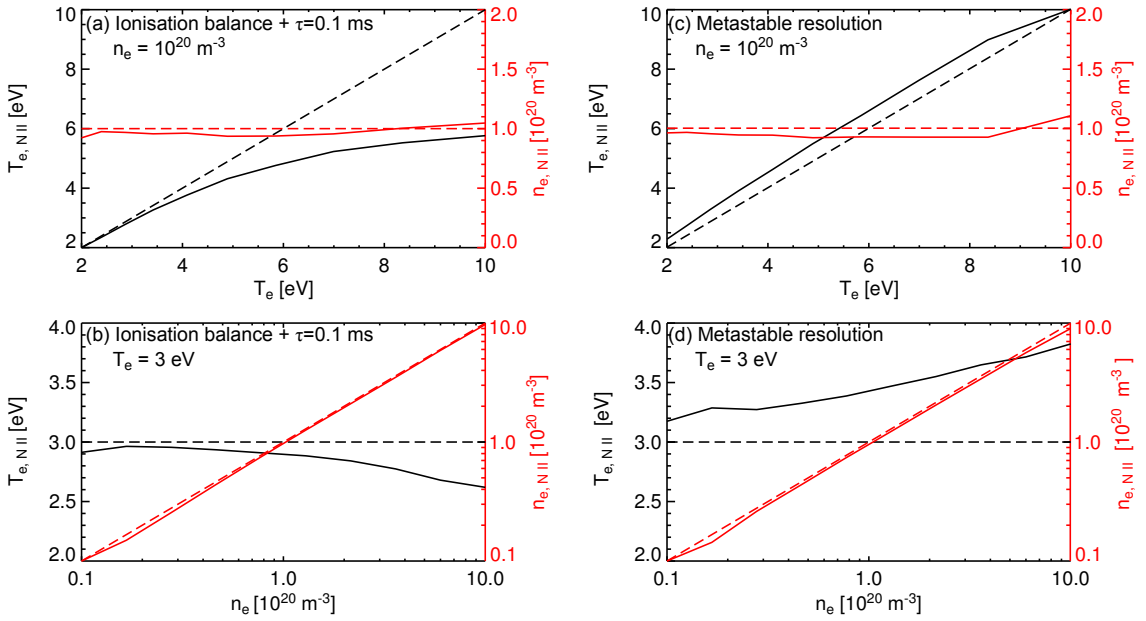

Figure 7. Synthetic modelled spectra are calculated using a single density of 10^{20} m^3 with a range of temperatures in (a) and (c) and a single temperature of 3 eV with a range of densities in (b) and (d). These pre-defined temperatures and densities are shown by the black and red dashed lines, respectively, in each figure. The modelled spectrum in (a) and (b) used an ionisation balance including a transport loss term ($\tau = 0.1$ ms) whereas the modelled spectrum in (c) and (d) use an ionisation balance in metastable resolution. The temperatures and densities calculated by applying the line ratio method to the synthetic spectrum are shown by the solid lines. The differences between the dashed and solid lines therefore indicate the error due to transport in (a) and (b) and due to using an unresolved ionisation balance in (c) and (d).

measurements. The dependency of the N III line ratio on T_e and n_e is also similar to the N II 404.1/399.5 nm line ratio which verify the similarities in the N II and N III line ratio measurements shown in figure 5.

To determine the electron temperature and density from the N II line ratio analysis, denoted as $T_{e,NII}$ and $n_{e,NII}$, a second least squares fit is applied to the fitted Gaussian and Voigtian line shapes using a model with free parameters of $T_{e,NII}$ and $n_{e,NII}$. Both the modelled and fitted spectrum are normalised to the 399.5 nm line so that the intensity, instrument function, and background are fixed. The T_e and n_e dependent model used to generate the spectrum in a form suitable for the FFS framework is called an ADAS Feature Generator (AFG). The implementation of the FFS-AFG fitting technique is further described by Nicholas [19] and is used routinely on JET.

3.4. Uncertainty

To test the uncertainty introduced by the unresolved, zero-transport ionisation balance, the emissivity of each line has been modelled at a range of T_e and n_e using a metastable resolved ionisation balance and an ionisation balance with a transport loss term, $n_e\tau$, described in [33]. The latter is used to mimic the scenario whereby impurity ions find

themselves in lower ionisation states than those obtained from ionisation balance due to reverse flow in the SOL [34], the ion temperature gradient force, or by charge exchange from a local source of neutral atoms. τ used in this analysis is estimated as 0.1 ms. The line ratio diagnostic (with an unresolved, zero-transport ionisation balance) is then used to assess the agreement with the input parameters.

Figure 7a-b shows the determined $T_{e,NII}$ and $n_{e,NII}$ values based on a modelled spectrum with τ included at constant n_e and varying T_e (a) and at constant T_e and varying n_e (b). The equivalent assessment based on a modelled spectrum with metastable resolved atomic rate coefficients is shown in figures 7c-d. The ionisation balance used in the line ratio diagnostic produces an uncertainty of 10% or lower for $n_{e,NII}$ over the full range of fusion relevant densities ($10^{19} - 10^{21}$ m^{-3}). For $T_{e,NII}$, the uncertainty from transport and metastables is low over the range $T_e = 2 - 4$ eV, consistent with the T_e from equilibrium ionisation balance, but may underestimate the temperature for $T_e > 4$ eV. The error bars shown on the determined $T_{e,NII}$ and $n_{e,NII}$ measurements in the following section are only representative of the least squares fitting uncertainty, which are dependent only on the uncertainty of measured radiance.

4. Results of line ratio analysis

It was shown in section 2.3 that the N II emission in ROV-14 spreads from the PFR into the SOL as T_{div} falls below ≈ 8 eV. If n_e is peaked in the PFR, as shown in previous modelling [12,35], then N II emission weighted more strongly to the PFR should sample a higher density than emission spread over both the PFR and SOL. The (inter-ELM) $T_{e,NII}$ and $n_{e,NII}$ measurements are shown in figure 8a and b as a function of time for sightlines ROV-14 (black) and ROV-12 (blue). For reference, T_{div} is shown by the red curve in figure 8a. The $T_{e,NII}$ from both sightlines remains consistently between $3 - 4$ eV suggesting that transport is not having a significant effect on the N II emission in this region of plasma.

The $n_{e,NII}$ in ROV-14 falls from $\approx 1.5 \cdot 10^{20}$ m^3 at $t = 2.5$ s to a value of $\approx 0.5 \cdot 10^{20}$ m^3 when T_{div} is at its lowest value of ≈ 3 eV at $t = 3.8$ s, whereas the $n_{e,NII}$ measurement in ROV-12 begins at a value of $\approx 0.5 \cdot 10^{20}$ m^3 at $t = 2.6$ s which increases to a value of $\approx 1.5 \cdot 10^{20}$ m^3 at $t = 3.8$ s. For ROV-12, it was shown in section 2.3 that the N II emission is sampling the PFR and SOL during the analysis time window. An increase in $n_{e,NII}$ indicates that either the PFR contribution to the N II emission is increasing, the PFR density is rising, or that the SOL density is increasing. The electron density from Stark broadening $n_{e,DI}$ shown in figure 8b is $3-4$ times greater than $n_{e,NII}$ and remains approximately constant in time which indicates that the PFR density is not changing significantly during the analysis time window. The LOS-based localization of the inter-ELM emission suggests that the PFR contribution is either decreasing or remaining approximately constant. Therefore, this measurement is most likely indicating that the N II emission sampled by ROV-12 is weighted more to the SOL as T_{div} decreases. Pressure conservation is still expected in the region of SOL plasma sampled by the N II

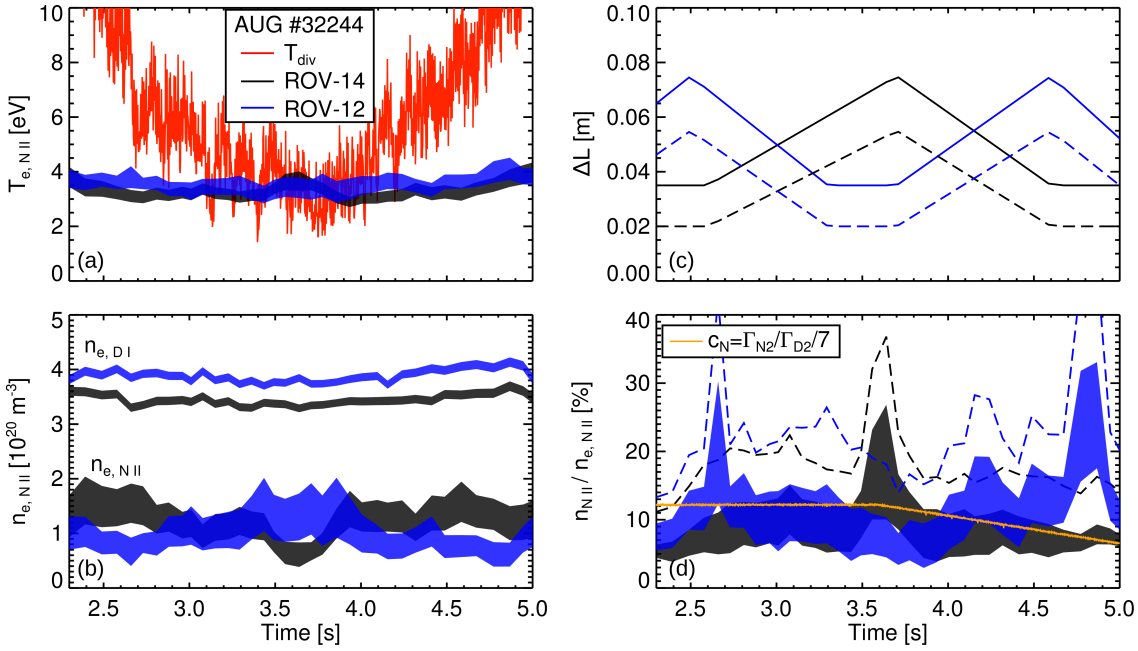

Figure 8. The plasma temperature and density measured using the N II line ratio analysis is shown in (a) and (b) respectively by the black (ROV-14) and blue (ROV-12) shaded regions. T_{div} and $n_{e,DI}$ are shown for comparison. The approximate N II emission lengths are shown in (c) with nitrogen concentrations shown in (d). The dashed lines represent the uncertainty based on ΔL, whereas the shaded regions represent the uncertainty due to the $n_{e,NII}$ and $T_{e,NII}$ measurements. The concentration based on the ratio of value fluxes is shown for comparison.

emission from ROV-12 and therefore the rise of $n_{e,NII}$ localised to the SOL is consistent with the fall of T_{div}. A subsequent drop in $T_{e,NII}$ is not found because the intensity of the N II emission in plasma temperatures below 3 eV falls below the detection threshold of the spectrometer. For example, there is no measurable N II emission from the inner divertor which is fully detached (i.e. $T_{div} < 1$ eV) during this analysis time window.

Lastly, by using the $n_{e,NII}$ measurements to constrain the N III line ratio, it is possible to provide an approximate measurement of $T_{e,NIII}$ corresponding to the N III emission. A value of $T_{e,NIII} \approx 10$ eV is found for both sightlines. Although not conclusive, given that $n_{e,NII}$ is not necessarily representative of the plasma where the N III is emitting, this temperature is moderately higher in comparison to the expected value of ≈ 6 eV from ionisation balance.

4.1. N II concentration

The N II density is calculated using the 399.5 nm spectral radiance because the population of the excited state driven by recombination is negligible. With this simplification, equation 1 can be re-written for the ion density as

$$n_{\sigma Z} = \frac{4\pi \int \epsilon_{j\to i} dS}{A_{j\to i} n_e f_{\sigma j}^{exc} \Delta L} \ [\mathrm{m}^{-3}] \qquad (2)$$

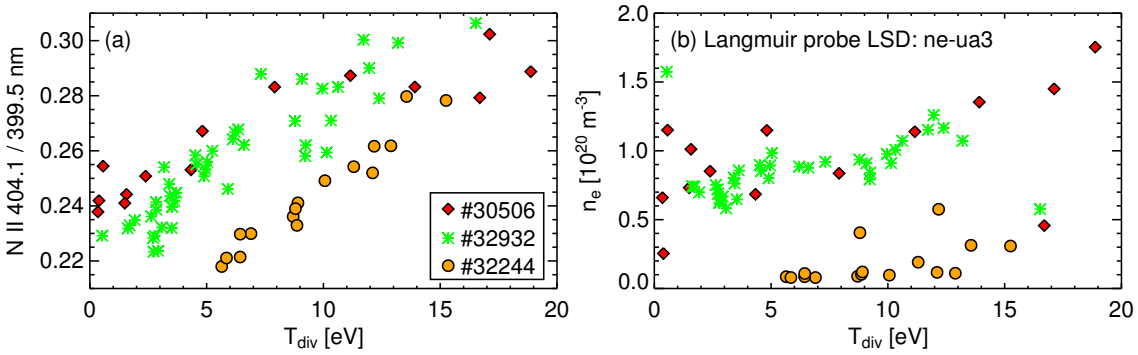

Figure 9. The N II 404.1 / 399.5 nm line ratio measured in ROV-13/14 as a function of T_{div} is shown in (a) over three different AUG discharges. The corresponding electron density from an outer divertor Langmuir probe is shown in (b).

where dS is the path length along the LOS and ΔL is the length of the emitting region. The N II concentration is defined as $c_{NII} = n_{NII}/n_{e,NII}$. The emitting zones shown in figure 3 suggest that the N II emission located in the PFR spans an approximate region of $2 - 3.5$ cm, whereas the N II emission located in the PFR and SOL covers approximately $5.5 - 7.5$ cm. In this approximation, the temporal evolution of ΔL is shown in figure 8c. The solid lines are used to demonstrate the concentration calculation described below, while the dashed lines are used to represent an approximate upper limit to the calculation. Constancy of c_{NII} over ΔL is also assumed because c_{NII} is peaked according to the product of n_e and n_Z.

Although the N II radiance at 399.5 nm at $T_{e,NII} = 3 - 4$ eV mostly represents the total atomic nitrogen content, molecular recombination is not included in the model and therefore c_{NII} is effectively a lower limit on the total atomic and molecular nitrogen content. The population of the upper state of this particular line may also be driven by molecular dissociation of either N_2, N_2^+, or NH_3 into an excited N II ion. Ammonia is mostly located in the recycling region close to the strike point, whereas N_2 will exist close to the puff location (in this case the PFR). Although the amount of emission driven by molecular dissociation is not yet well characterised, it has been found that the ratios do not vary significantly during a period of constant T_{div} but with varying seeding rates (including a period of zero seeding).

With the approximate form of ΔL, the c_{NII} is shown in figure 8d to vary between $\sim 5 - 25$ % in the analysed discharge and shows agreement over both ROV-12 and ROV-14. The shaded regions represent the uncertainty from $n_{e,NII}$ and $T_{e,NII}$ while the dotted lines include the uncertainty in ΔL. Usually c_Z is estimated in AUG in constant conditions using the ratio of valve fluxes $c_N = \Gamma_Z/\Gamma_D/Z$ [36]. This approximation for c_N is also shown in figure 8d and agrees within the error bars of the spectroscopic measurements.

4.2. Implementation

Spectral diagnostics of the sort described in this paper can either be used as a control-room diagnostic or as a modelling constraint for SOL codes. In the case of the former, it is important to find trends that are robust across a number of discharges and that are reasonably independent of the uncertainties described in sections 3 and 3.4. Furthermore, fitting a particular weak line in a spectrum is often challenging and can require more time than is available between two discharges. One result which appears robust is the correlation between the 404.1 / 399.5 nm line ratio and T_{div}. Figure 9a shows the line ratio measured in ROV-13/14 as a function of T_{div} measured over three AUG discharges. To a first-order approximation, the N II ratio value begins to decay as T_{div} falls below 15 eV. The scatter between the discharges is due to the differences in n_e as shown in figure 9b. For a lower n_e, the N II ratio value is lower in agreement with figure 6a. This spectral signature could therefore provide an additional indication that the outer divertor is evolving either into or out of a partially detached state. Furthermore, the two N II lines are relatively bright and therefore an accurate fit of the radiance can be obtained, in most cases, on first attempt.

To use the measured $T_{e,NII}$ and $n_{e,NII}$ as a modelling constraint, a synthetic sightline spectrum must be generated by a SOL model, such as SOLPS, and then assessed in the same manner as the experimental spectra. Without this process of comparison, it is difficult to assign a single radial or vertical location for the measurement since the emission, even when described as *localised*, still spans a finite ΔL. Furthermore, a direct comparison of the measured and synthetic spectrum could be assessed without any further post-processing, however any differences due to changes in the plasma background are then harder to interpret. The modelled spectrum should incorporate the balance of N II and N III with values determined using both atomic physics and plasma transport. The AFG model used to fit the spectrum (discussed in section 3) can also be used for this purpose; although it uses an ionisation balance as default, it can replace this with an N II and N III population as input.

5. Conclusions

The divertor spectrometer on ASDEX Upgrade routinely measuring the Stark broadening of the D_θ and D_ϵ lines can also measure a number of N II and N III lines sensitive to the background plasma temperature and density. A model of the N II line ratio density and temperature dependence is presented based on a combination of new and previously published atomic data. Measurements of the inter-ELM N II and N III radiance from sightlines viewing horizontally across the outer divertor plasma are shown during a divertor temperature scan from $\approx 3 - 20$ eV in a partially detached ELMy H-mode plasma. It is shown using a line-of-sight localisation of spectrometer radiance measurements that the emission closer to the X-point spreads from the private flux region into the scrape-off-layer as the divertor temperature decreases, whereas the

emission closer to the strike point is sampling both the private flux region and scrape-off-layer throughout the analysis time window. This is consistent with the evolution of the density measurements obtained by N II line ratio analysis. The N III line ratio in this spectral range cannot be used to obtain a single solution of the temperature and density, however by using the density determined using the N II line ratio measurements an approximation of the N III temperature can be obtained. A model of the emitting region length has been presented and used in combination with the radiance measurements and atomic data to calculate the nitrogen divertor concentration. For this discharge, the concentration is determined to be $5 - 25\%$ in the outer divertor during partial detachment. In summary, the nitrogen line ratio technique can be implemented solely as a control room diagnostic, but would provide a more thorough description of the divertor plasma coupled with inverted filtered camera measurements to determine the length (and location) of the emitting region or by comparisons with a synthetic diagnostic model.

Acknowledgements

S. Henderson would like to thank H. Summers for helpful discussions. B. Lipschultz was funded in part by the Wolfson Foundation and UK Royal Society through a Royal Society Wolfson Research Merit Award as well as by the RCUK Energy Programme (EPSRC grant number EP/I501045). This work has been carried out within the framework of the EUROfusion Consortium and has received funding from the Euratom research and training programme 2014-2018 under grant agreement No 633053. Work performed under EUROfusion WP MST1. The views and opinions expressed herein do not necessarily reflect those of the European Commission.

Appendix A. Autostructure optimisation

Using default *autostructure* for near neutral ions, such as N II, can produce unsatisfactory uncertainties in the atomic data. The solution can be improved by optimising a dimensionless radial scaling parameter for each nl-orbital such that a user-specified weighted sum of eigenenergies is minimised. An optimisation approach similar to previously described methodologies [28, 37] is adopted in this paper. The radial scaling parameters were firstly optimised using the internal least squares approach within *autostructure*. These parameters were then adjusted to optimise the level energies of

Table A1. Radial scaling parameters for each nl orbital.

n	s	p	d	f
1	1.45	-	-	-
2	1.33	1.28	-	-
3	1.33	1.28	1.22	-
4	1.00	1.22	1.22	1.23

the $2s^2 2p4f$ configuration. The electron configuration set underpinning the calculation matches that of Tayal and includes the additional 2p4d, 2p4f configurations, for the spectral analysis, and the $1s^2 2p^4$ and $2s2p^2 3p$ configurations for core polarisation. The optimised parameters for each *nl* orbital are shown in table A1.

Appendix A.1. Data archiving

The calculations were carried out within the ADAS framework and are available via OPEN-ADAS at `http://open.adas.ac.uk`. Source and output data are stored in ADAS data format (*adf*) files for which the formal format specification is documented on the ADAS website. The fundamental source data for the atomic energy levels, *A*-values, and effective collision strengths are archived in *adf04* files, which are separate files for N II and N III in *ls* resolution. The year 96 *adf11* data sets of ionisation and recombination rate coefficients are used to calculate the equilibrium ionisation balance.

References

[1] L. Aho-Mantila *et al.*, Nucl. Fusion **52**, 103006 (2012).
[2] F. Reimold *et al.*, J. Nucl. Mater. **463**, 128 (2015).
[3] E. Havlickova *et al.*, Plasma Phys. Control. Fusion **57**, 115001 (2015).
[4] S. Potzel *et al.*, Plasma Phys. Control. Fusion **56**, 025010 (2014).
[5] B. Lomanowski *et al.*, Nucl. Fusion **55**, 123028 (2015).
[6] A. Pigarov, J. L. Terry, and B. Lipschultz, Plasma Phys. Control. Fusion **40**, 2055 (1998).
[7] J. A. Goetz *et al.*, Phys. Plasmas **6**, 1899 (1999).
[8] P. Monier-Garbet *et al.*, Nucl. Fusion **45**, 1404 (2005).
[9] A. Kallenbach *et al.*, Plasma Phys. Control. Fusion **55**, 124041 (2013).
[10] M. Bernert *et al.*, Nucl. Mater. Ener. **in press**, (2017).
[11] D. Brunner *et al.*, Nucl. Fusion **57**, 086030 (2017).
[12] F. Reimold *et al.*, Nucl. Fusion **55**, 033004 (2015).
[13] M. Reinke *et al.*, Nucl. Mater. Ener. **in press**, (2017).
[14] R. J. Goldston, M. L. Reinke, and J. A. Schwartz, Plasma Phys. Control. Fusion **59**, 055015 (2017).
[15] M. Reinke, Nucl. Fusion **57**, 034004 (2017).
[16] A. Kallenbach *et al.*, Plasma Phys. Control. Fusion **52**, 055002 (2010).
[17] A. Kallenbach *et al.*, Nucl. Fusion **55**, 053026 (2015).
[18] National Institute of Standards and Technology (NIST) Atomic Spectra Database.
[19] C. H. Nicholas, Ph.D. thesis, University of Strathclyde, 2011.
[20] J. McCarthy, Commun. Assoc. Comp. Mach. **3**, 184 (1960).
[21] R. Prakash *et al.*, IPP-10/31 (2006), Max-Planck-Institut für Plasmaphysik (unpublished).
[22] M. Carr *et al.*, 44th EPS conference on Plasma Physics, Belfast, Ireland O5.130 (2017).
[23] H. P. Summers *et al.*, Plasma Phys. Control. Fusion **48**, 263 (2006).
[24] S. S. Tayal, Astrophys. J. Suppl. Ser. **195**, 12 (2011).
[25] P. R. Young *et al.*, Astrophys. J. Suppl. Ser. **144**, 135 (2003).
[26] C. E. Moore, Technical report, Nat. Stand. Ref. Data Ser., NSRDS-NBS 3 (Sect. 5), 80 pp. (Nat. Bur. Stand., U.S., 1975) (unpublished).
[27] N. R. Badnell, Comput. Phys. Commun. **182**, 1528 (2011).
[28] M. A. Bautista *et al.*, Astron. Astrophys. **508**, 1527 (2009).
[29] P. J. Storey and T. Sochi, Mon. Not. R. Astr. Soc. **459**, 2558 (2016).
[30] R. P. Stafford, K. L. Bell, and A. Hibbert, Mon. Not. R. Astr. Soc. **266**, 715 (1994).

[31] K. L. Bell, A. Hibbert, R. P. Stafford, and T. Brage, Mon. Not. R. Astr. Soc. **272**, 909 (1995).
[32] R. D. Cowan, The Theory of Atomic Structure and Spectra (University of California Press, Berkeley, 1981).
[33] P. G. Carolan and V. A. Piotrowicz, Phys. Plasmas **25**, 1065 (1983).
[34] P. C. Stangeby and G. M. McCracken, Nucl. Fusion **30**, 1225 (1990).
[35] P. C. Stangeby, J. D. Elder, A. G. McLean, and J. G. Watkins, Nucl. Mater. Ener. **in press**, (2017).
[36] A. Kallenbach and the ASDEX Upgrade Team, Nucl. Fusion **57**, 102015 (2017).
[37] D. Kasen, N. R. Badnell, and J. Barnes, Astrophys. J. **774**, 13 (2013).